Comparing granular and fragmentation-driven silo DEM models for block caving

Manuel Cárdenas-Barrantes, Mathieu Renouf, Emilien Azéma, Carlos Ovalle

Powder Technology 476 (2026) 122409

Contents lists available at ScienceDirect

Powder Technology

journal homepage: www.journals.elsevier.com/powder-technology

Comparing granular and fragmentation-driven silo DEM models for block caving

Manuel Cárdenas-Barrantes [a,b,c,*], Mathieu Renouf [d], Emilien Azéma [a,d], Carlos Ovalle [a,b]

[a] Department of Civil, Geological and Mining Engineering, Polytechnique Montreal, Quebec, Canada
[b] Research Institute on Mining and Environment (RIME), UQAT-Polytechnique, Quebec, Canada
[c] 3SR, Université Grenoble Alpes, CNRS, Grenoble, France
[d] LMGC, Université de Montpellier, Montpellier, France

HIGHLIGHTS

- Granular discharge obeys Beverloo scaling regardless of particle shape and packing density.
- Particle interlocking strongly reduces flow rate and caveability.
- Stress redistribution differs fundamentally between disks and fragmented blocks.
- Fragmentation-driven packings sustain quasi-static cave-shaped flow zones.

GRAPHICAL ABSTRACT

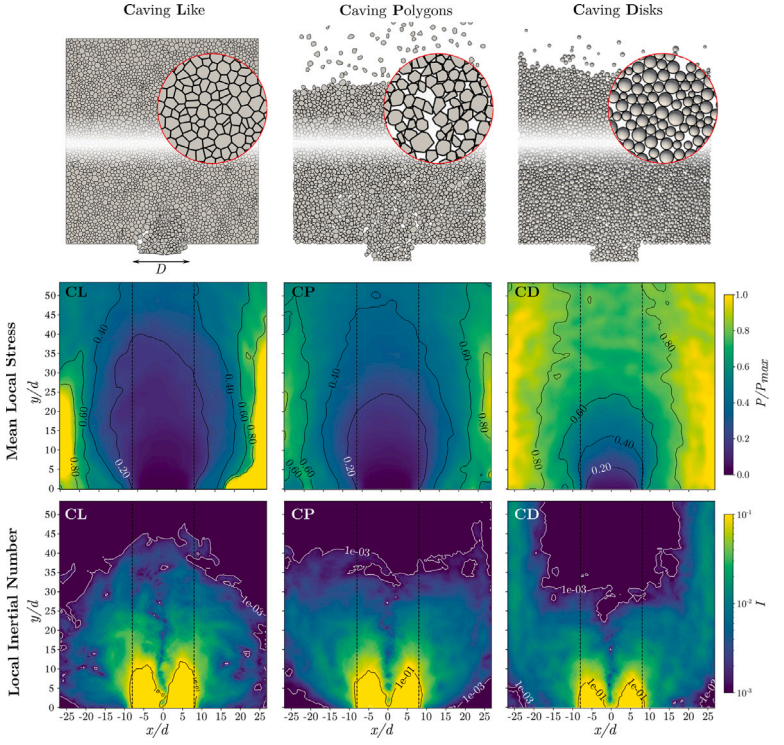

ARTICLE INFO

Keywords:
Block caving
Discrete-element modeling
Silo

ABSTRACT

Silo analogies are commonly used in block caving research to study gravity-driven flow and stress redistribution. However, most existing models rely on idealized granular assemblies composed of random granular packings, which might differ from fragmented rock masses. The aim of this numerical study is to investigate the influence of material characteristics on flow dynamics and internal stresses in a silo. Using the Discrete Element

* Corresponding author at: Department of Civil, Geological and Mining Engineering, Polytechnique Montreal, Quebec, Canada.
E-mail addresses: manuel.cardenas@univ-grenoble-alpes.fr (M. Cárdenas-Barrantes), carlos.ovalle@polymtl.ca (C. Ovalle).

https://doi.org/10.1016/j.powtec.2026.122409
Received 13 January 2026; Received in revised form 24 February 2026; Accepted 10 March 2026
Available online 11 March 2026

Fragmentation
Granular gravity flow

Method (DEM), we compare three silo models: (i) a *caving-like* (CL) configuration, generated by progressively de-bonding a tessellated solid column during draw, thus emulating rock fragmentation; (ii) a *caving-polygons* (CP) configuration, in which the same fragments are deposited randomly into the silo; and (iii) a *caving-disks* (CD) configuration, representing a traditional granular silo composed of circular particles; all three models share the same particle size distribution. These configurations enable comparing the effects of granular packing, particle shape, interlocking, and fragmentation mechanisms on discharge behavior. Results show that flow velocities, displacement fields, and internal pressure distributions differ markedly between traditional granular silos and fragmentation-driven systems. The CD configuration develops the highest pressures surrounding the outlet, whereas the CL configuration redistributes stresses more efficiently, with forces preferentially supported by the silo walls; the CP system exhibits intermediate behavior.

The findings highlight key limitations of conventional silo analogs and underscore the need for more representative material descriptions in block caving simulations. This work provides a basis for selecting appropriate DEM modeling strategies, with perspectives of improving DEM cave-flow predictions.

1. Introduction

Block caving is the most efficient and cost-effective underground mining method for extracting large, low-grade ore bodies at depth [1]. Caving relies on the ability of the ore column to fragment, collapse, and flow under gravity as material is progressively extracted from drawpoints. Understanding the evolution of the caved rock mass (e.g., its fragmentation, flow behavior, and the associated stress redistribution) remains essential for improving safety, draw control, and production planning [2–5].

Failures associated with draw extraction damage [6], air-gap collapse [7] and rockbursts [8] have highlighted persistent operational hazards in cave mining. These events emphasize the need for reliable design methods to ensure safe and efficient mining operations. Due to inherent uncertainties and complexities of the caving process, empirical design methods have been established [3,9,10]. These widely applied approaches were developed from operational experience, case histories, and large datasets from major caving mines [5]. Physical modeling has also played a key role in understanding gravity flow during caving. Laboratory studies have used silo analogs to reproduce granular discharge from caved material [11,11–14]. These scaled models have demonstrated flow features directly relevant to block caving, including formation of isolated extracted zones, dilution, and drawpoint interaction. However, while silos effectively capture gravity-driven flow, they fail to represent critical mechanisms such as in-situ fragmentation, breakage patterns, arching, and the evolving mechanical response of the collapsing rock column. This has motivated the need for more representative physical models, such as centrifuge testing of caving processes [15].

The multi-scale nature of caving processes has led to the implementation of various advanced numerical approaches, including kinematic models to assess caved rock flowability [3,16], Smoothed Particle Hydrodynamics for modeling cave initiation and propagation [17], Finite Element Methods to evaluate stress–deformation responses around the cave [7,18], and Discrete Fracture Network approaches that explicitly represent persistent joints and fragmentation [19,20]. However, these methods do not always capture the defining characteristics of gravity-driven granular flows, which are more effectively represented by particle-based approaches. The Discrete Element Method (DEM) has therefore been widely used to simulate granular flow kinematics, including fines migration and dilution [13,21,22]. Nevertheless, conventional particle-based DEM struggles to adequately represent caveability and the associated stress field evolution. Alternatively, block-based DEM formulations using deformable blocks bonded by joints, such as UDEC [23], allow the simulation of crack propagation and arching, and capture the influence of joint orientation and persistence on caveability [24–26]. Yet, these approaches fail to reproduce the essential characteristics of gravity-driven granular flow. Therefore, a persistent challenge remains in ensuring the representativeness of the granular analogs used to model caving processes, and there is a clear need for alternative modeling strategies capable of simultaneously capturing granular-flow kinematics and the geomechanical response of the caved rock mass.

Following this motivation, the present study performs a systematic comparison of three distinct DEM representations of a caving column modeled as a silo. The first configuration uses a tessellated 2D solid block that fully fills the silo and undergoes disassembling to mimic fragmentation; the tessellation is constructed with a prescribed particle size distribution (PSD). Thus, once extraction starts from the drawpoint, the model captures fragmentation through unbonded block deconstructuction, which collapses into smaller pieces and flow under gravity. The second configuration employs the same fragments as the tessellated block, but arranges them as a random granular assembly into the silo. A third configuration corresponds to a traditional 2D granular assembly of disks, which is constructed to exactly match the PSD of the previous cases. The approach compares samples with the same PSD, but different fragment shapes, initial packings, and formation histories. The results are analyzed in terms of caveability, flow characteristics, and stress distributions.

This manuscript is organized as follows: Section 2 describes the numerical DEM approach used to create two-dimensional silos of tessellated solid, polygons and disks. Section 3 presents the results and discussions, focusing on gravity flow, stress distribution and caveability. Finally, Section 4 concludes and raises perspectives on this work.

2. Methodology and numerical procedure

We performed two-dimensional numerical simulations of silo discharge with rigid boundaries using the Contact Dynamics method. We investigated the discharge behavior of three distinct granular configurations: (i) a block-caving-derived tessellation into unbonded polygonal particles, (ii) a disordered arrangement of the same polygons generated by random gravitational deposition, and (iii) a packing of disks that preserves the equivalent size and mass of the original polygonal grains. From this point onward, we refer to these configurations as *caving-like* (CL), *caving-polygons* (CP), and *caving-disks* (CD) systems, respectively. The simulations are conducted in two dimensions as a methodological choice. Although quantitative differences between 2D and 3D systems are expected, the fundamental mechanisms governing granular flow, arch formation, contact network evolution, and stress redistribution remain qualitatively similar. Two-dimensional DEM simulations have been widely used to investigate force chains, arching, and confined granular flow in geomechanical contexts [27–31]. The 2D framework enables systematic exploration of particle shape and initial structure at a significantly lower computational cost, allowing us to identify robust mechanisms and trends expected to remain valid across dimensions.

The numerical simulations were carried out using the open-source software LMGC90 [32,33], which solves the equations of motion for rigid bodies through an implicit non-smooth formulation. Contact forces and particle velocities are obtained iteratively using a nonlinear Gauss–Seidel scheme [34,35]. The Contact Dynamics method enables

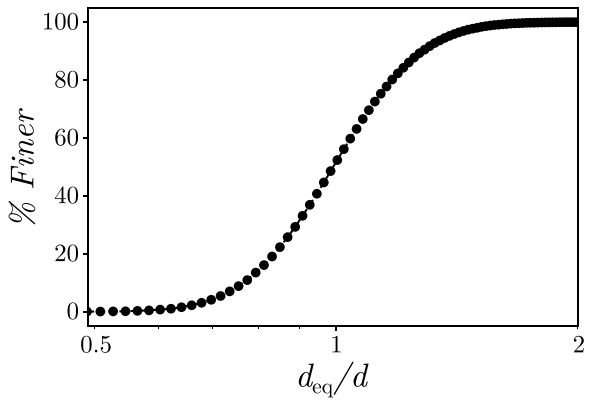

Fig. 1. Particle size distribution (PSD) over all samples (CL, CP and CD).

accurate simulations of systems exhibiting a wide range of particle shapes and high size polydispersity.

CL is generated by tessellating a rectangular domain into 2×10^4 polygonal particles using the Software Neper [36]. This approach has been successfully used to model the fragmentation of discrete media, including the behavior of crushable granular materials [37], anisotropic fracture persistence [38], and size effects on rock strength [39]. The width of the tesselated domain is $W \approx 56d$ and its height is $H = 6W$, where d is the mean equivalent diameter of the grains resulting from the tesselation. The equivalent diameter of each grain is computed as $d_{eq} = \sqrt{\frac{4A}{\pi}}$, with A the area of the polygonal particle. The PSD of the polygons is represented by a normal distribution, with a polydispersity $\lambda = \frac{d_{eq,90}}{d_{eq,10}} = 1.66$, where $d_{eq,90}$ and $d_{eq,10}$ are the equivalent diameters from which 90% and 10% of the particles are finer, respectively. Fig. 1 shows the resulting PSD. The mean particle roundness, defined as $R = \frac{c^2}{4\pi A}$, with c the particle perimeter and A its area, is 0.90 ± 0.05. R quantifies how close the particle shape is to a circle, with $R = 1$ being a disk. Note that, by construction, the initial packing fraction of this configuration is $\phi = 1$ (with ϕ the volume of solid over the total volume), as highlighted in the red zoomed-in view in Fig. 2a. Finally, the particles interact through purely frictional contacts (i.e., without bonding).

CP uses exactly the same polygonal particles as CL, but is generated by random deposition under gravity in a box of width W, producing a disordered packing with a height in average 1.2 times that of the CL configuration (see Fig. 2b). Logically, the solid fraction is lower than in CL, with average $\phi = 0.80$ (see Fig. 2b). Finally, CD consists of circular particles with diameters equal to the equivalent diameters of the polygons in CL (i.e., the same area and PSD), placed randomly under gravity in a box of width W. In this case, the resulting height is lower than that of CP, reaching in average 1.1 times the height of CL, with $\phi = 0.86$ (see Fig. 2c).

As shown in Fig. 2, an outlet door of width D is positioned at the center of the bottom boundary of each configuration, allowing particles to flow as in a silo. To guarantee sufficiently large samples and steady-state flow in both CP and CD, a refilling procedure was implemented. Any particle that exited the door and reached a distance of $0.5W$ below it, was randomly reintroduced into a $W \times 0.5W$ region at the top of the silo immediately above the highest stable particle (see Figs. 2b and c) [40].

Since $H \gg W$, particle reintroduction does not influence the dynamics near the outlet nor the stresses at the silo base, where measurements are performed, as stress saturation is ensured by the Janssen effect [40–43]. This allows CP and CD to maintain a statistically stationary flow over extended time windows. For CL, the refilling procedure was not applied in order to preserve the geometrical unity of the system. Nevertheless, the simulations naturally reach a steady-flow regime for a sufficiently long period of time to allow reliable measurements. To ensure statistical robustness, 25 independent simulations were performed for CL for each door size, whereas three independent realizations were conducted for CP and CD for each door size.

Table 1
Simulation parameters.

Parameter	Symbol	Value
Gravity	g	9.81 ms^{-2}
Particle Mass Density	ρ	$2.7 \cdot 10^3$ kgm^{-2}
Mean Particle Diameter	d	0.0188 m
Maximum Particle Diameter	d_{max}	$2.6d$
Minimum Particle Diameter.	d_{min}	$0.36d$
Friction Coefficient	μ	0.4
Width and Height	W, H	$56d$, $6W$
Number of Particles	N	$2 \cdot 10^4$

The friction coefficient was fixed at $\mu = 0.4$ for particle–particle and particle–wall interactions in all configurations. Simulations were conducted for several normalized door widths: $\frac{D}{d}$ = [8, 10, 12, 14, 16, 18, 20, 22, 24, 26]. Table 1 summarizes the main parameters of the simulations. Keeping the same PSD between different configurations, our framework allows a direct comparison of the effects of particle shape, packing order, and initial fabric on the discharge behavior, linking silo observations to flow mechanisms relevant in block-caving operations.

3. Results and discussion

3.1. Gravity flow

The flow rate was obtained by following the evolution in time of the cumulative number of particles $N(t)$ exiting the silo. Figs. 3a–c show representative examples of $N(t)$ for CL, CP and CD for different door sizes D/d, plotted from dark purple to light yellow in ascending order. Time is normalized by the characteristic scale $t_0 = \sqrt{d/g}$. The cumulative count $N(t)$ is normalized by $N^* = 16212$, 13871, and 33139, which is the total number of particles discharged at $t/t_0 = 2200$ (~95 s) for the smallest opening, for the CL, CP, and CD configurations, respectively. Note that particle refilling is implemented only in the CP and CD cases.

In cases where a clog occurred, it was cleared by removing the particle closest to the center of the outlet [40,43]. Clogging events were identified from a near-complete loss of kinetic energy, detected numerically when $K_{t_{n-1}}/K_{t_n} < 10^{-3}$. As expected, clogging was predominantly observed for the smallest outlet openings, consistent with previous studies showing that constriction size and particle shape strongly influence the probability of interlocking and therefore arch formation [42, 44]. As commonly reported in granular flow studies [21,40,45], the function $N(t)$ increases monotonically with time for all configurations, with its slope defining the flow rate Q, which increases with door opening size.

The onset of the stationary regime depends on both D and the packing configuration. For CL, a steady state is reached at t/t_0 = [500, 400, 200, 300, 150, 150, 80, 70, 60, 50] for the corresponding door sizes D/d in ascending order. For CP and CD, both with refilling procedure, we set $t/t_0 = 1000$ as the onset of steady flow, after which the discharge rate remains constant.

Fig. 4 presents the flow rate as a function of the normalized outlet size D/d. The values shown correspond to the mean flow rate over all simulated samples in the stationary regime, normalized by the CL flow rate with the largest aperture $Q^* = 2182$ particles/s. For all D studied, CD yields discharge rates substantially higher than the other two cases, with the difference becoming more pronounced at larger apertures. The differences are attributed to particle shape, as polygonal grains develop geometric interlocking that resists gravity-driven motion. This effect is stronger in CL, where both the packing fraction and the structural configuration enhance resistance to flow. Consequently, representing block

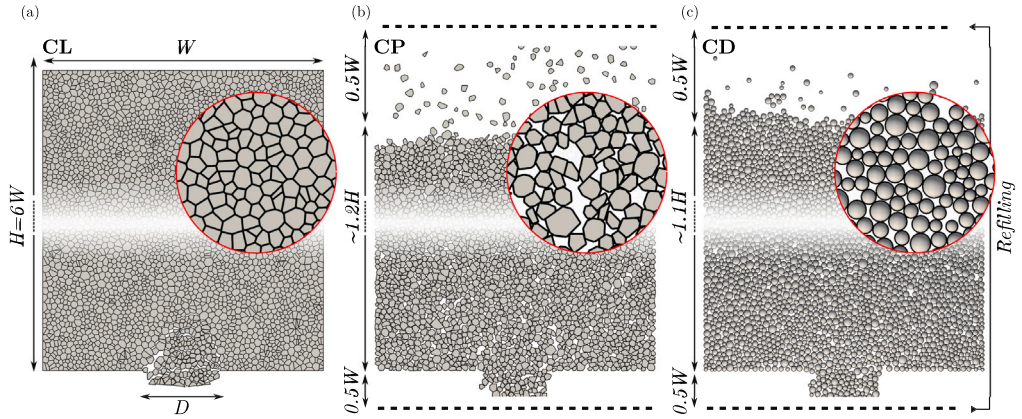

Fig. 2. Methodology and numerical setup of the simulations. Panels (a), (b), and (c) correspond to the CL, CP, and CD configurations, respectively. Red circular insets zoom in the arrangement and shape geometry of the particles.

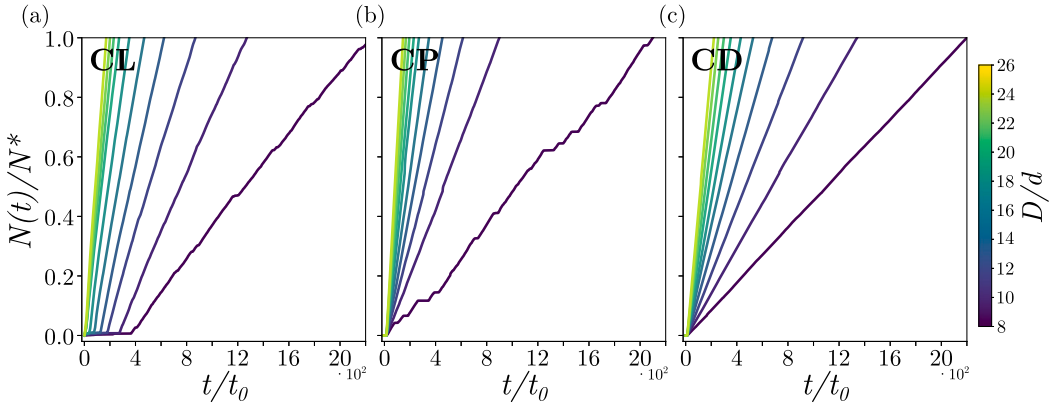

Fig. 3. Time evolution of the cumulative number of discharged particles, $N(t)$, for: (a) CL, (b) CP, and (c) CD. Curves correspond to different door sizes D/d, plotted from dark purple to light yellow in ascending order. The cumulative count $N(t)$ is normalized by $N^* = 16212$, 13871, and 33139, the total number of particles discharged at $t/t_0 = 2200$ (~95 s) for the smallest opening, for the CL, CP, and CD configurations, respectively.

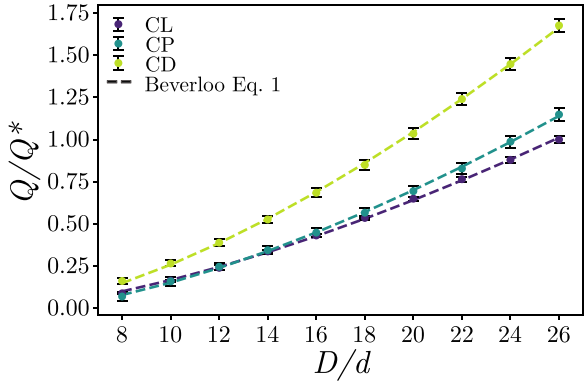

Fig. 4. Flow rate Q/Q^* as a function of the normalized outlet size, D/d, for CL, CP and CD. Q^* corresponds to the flow rate of CL for the largest aperture. The dashed lines correspond to the best fit of the Beverloo equation, Eq. (1).

caving with silos composed of particles that lack the initial geometric unity of a fractured rock mass leads to a systematic overestimation of the discharge rate. This occurs even when the PSD and particle shapes are identical, but the particles are arranged in a random manner. such as CL and CP. CL and CP, for small D, both exhibit nearly identical flow rates, but with their behavior progressively diverging as the size of the door increases.

The dashed lines in Fig. 4 correspond to fits using the Beverloo equation [46,47]:

$$Q = C\,\rho\, g^{1/2}\,(D - k\,d)^{3/2}\,, \tag{1}$$

where C is a dimensionless prefactor associated with the velocity field near the outlet, particle polydispersity, and particle shape, and k is a geometrical factor accounting for an effective outlet size smaller than the physical opening. Here, ρ is the particle mass density. The fitted values are $C = (0.9, 1.1, 1.5)$ and $k = (3.1, 4.4, 3.5)$ for the CL, CP, and CD configurations, respectively. The lower value of C for CL reflects a reduced flow-rate scale due to enhanced interlocking and arching of angular particles, which reduce particle mobility near the outlet. The velocities are larger for CD than for CL, with CP taking intermediate values, consistent with the observed variation in C. These results further demonstrate the dependence of the discharge rate on both particle shape and the initial packing structure. No clear monotonic trend is observed for k. This geometrical factor depends on both particle shape and packing density: angular particles tend to reduce the effective outlet section (larger k) due to stronger excluded-volume and arching effects, whereas higher packing density can counterbalance this reduction by the closer particle arrangements near the outlet, effectively increasing $(D - kd)$. This interpretation is a preliminary hypothesis, and a systematic study of particle shape from highly angular to circular would be needed to fully separate shape and packing effects.

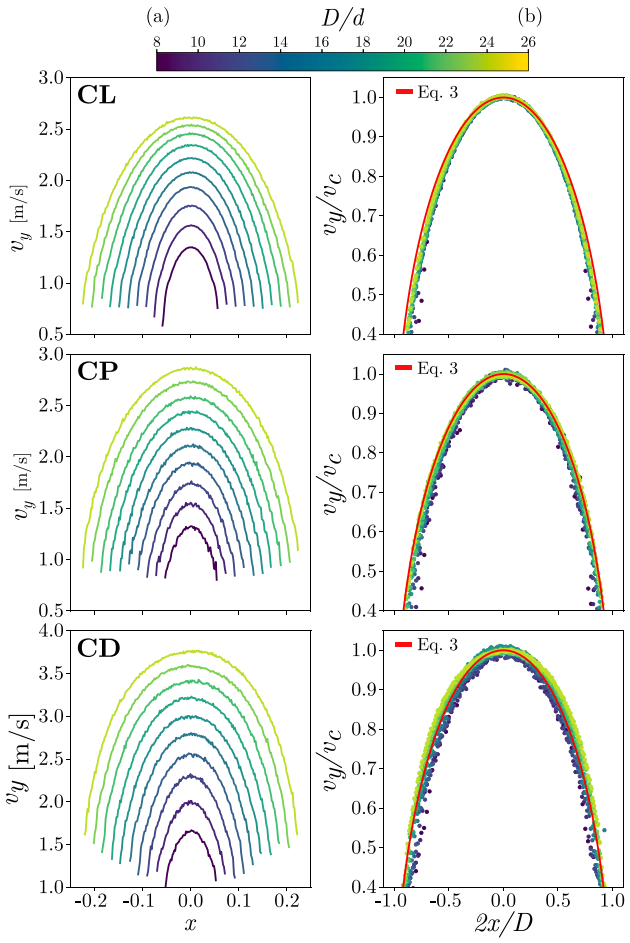

Fig. 5. (a) Vertical velocity profiles at the outlet for different opening sizes (dark purple to light yellow) and for the three configurations from top to bottom: CL, CP, and CD. (b) Corresponding normalized vertical velocity profiles, where the vertical velocity is scaled by the central velocity at the outlet and the horizontal coordinate is scaled by half the outlet width. When rescaled, all profiles collapse onto a single master curve, with the red line representing the best fit to Eq. (3).

To further study the gravity flow behavior, we analyze the velocity field of the particles at the outlet. The velocity distribution was obtained by dividing the outlet region into bins of width $\Delta x = 0.1d$ and computing the mean vertical velocity v_y of the particles exiting through each bin. In this calculation, the mean value corresponds to the combined set of all particles passing through the outlet during the steady-flow regime across all samples. Fig. 5 presents the resulting velocity profiles for the outlet sizes, colored from dark purple to light yellow in ascending order, and for the three configurations. As expected, the vertical velocity profiles exhibit a parabolic shape [47], with a maximum at the center of the outlet ($x = 0$) that increases systematically with D.

Fig. 6 displays the velocity at the center of the outlet for each configuration. Following the trend observed for the discharge rate, the central velocities are higher in CD, intermediate in CP, and lower in CL, with the latter two being relatively similar. The data follow a power-law relation given by

$$v_c = \beta\sqrt{gD}, \tag{2}$$

which arises from a free-fall energy argument for particles located at the centerline of the silo [40,45,47]. The factor β scales the velocity according to the geometrical and frictional properties of the particles [47]. In this study, we obtained $\beta = (0.16, 0.17, 0.22)$ in CL, CP and CD, respectively, highlighting the reduced kinetic energy of particles discharging in the CL configuration compared to the other two cases.

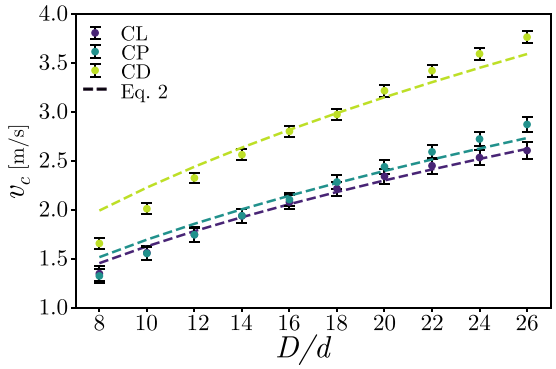

Fig. 6. Central vertical velocity v_c as a function of outlet size D for the three configurations. CD exhibits the highest velocities, followed by CP and CL. The solid line corresponds to the power-law fit $v_c = \beta\sqrt{gD}$.

The self-similar behavior of the velocity profiles was examined by normalizing the vertical velocity by the corresponding central value v_y/v_c, and the horizontal position by half the width of the outlet $x/(D/2)$ [47]. For all three configurations, the normalized profiles collapse onto a single master curve, independent of D, as shown in Fig. 5b. This curve is well described by the functional form [47]

$$\frac{v_y}{v_c} = \left(1 - \frac{2x}{D}\right)^{1/2}, \tag{3}$$

confirming that, despite clear quantitative differences in flow rate and velocity magnitude, the overall dynamical behavior remains qualitatively similar across all three cases. In other words, particle geometry and initial structural arrangement affect the discharge quantitatively, but do not modify the fundamental flow mechanism that governs the velocity field at the outlet.

3.2. Stress distribution

To better understand the dynamical and mechanical properties of the particle flow, we compute continuum fields using a coarse-graining methodology [48,49]. Coarse-graining provides a consistent way to transform discrete particle data into smooth macroscopic fields. Following [45], the macroscopic mass density of the granular flow, $\eta(\mathbf{r}, t)$, is defined as

$$\eta(\mathbf{r}, t) = \sum_{i=1}^{N} m_i G\left(\mathbf{r} - \mathbf{r}_i(t)\right), \tag{4}$$

where the sum runs over all particles and $G(\mathbf{R})$ is the coarse-graining function. In this study, we use a truncated Gaussian coarse-graining function,

$$G(\mathbf{R}) = \frac{1}{2\pi d^2} \exp\left[-\left(\frac{|\mathbf{R}|}{\sqrt{2}d}\right)^2\right], \tag{5}$$

with a cutoff radius $r_c = 3d$.

Following this coarse-graining approach, the stress tensor $\sigma_{\alpha\beta}(\mathbf{r})$ is defined as

$$\sigma_{\alpha\beta}(\mathbf{r}) = \frac{1}{2}\sum_{i=1}^{N}\sum_{j=1}^{N_{c_i}} f_{ij}^{\alpha} r_{ij}^{\beta} \int_0^1 G\left(\mathbf{r} - \mathbf{r}_i + s\mathbf{r}_{ij}\right) ds, \tag{6}$$

where the sum N run over all the particles i, and the sum N_{c_i} runs over the contacting particles j of i, with $\mathbf{r}_i$ and $\mathbf{r}_j$ their respective positions. $\mathbf{r}_{ij} \equiv \mathbf{r}_i - \mathbf{r}j$ is the branch vector and $\mathbf{f}_{ij}$ is the force exerted by particle j on particle i. In this definition, the kinetic contribution to the stress

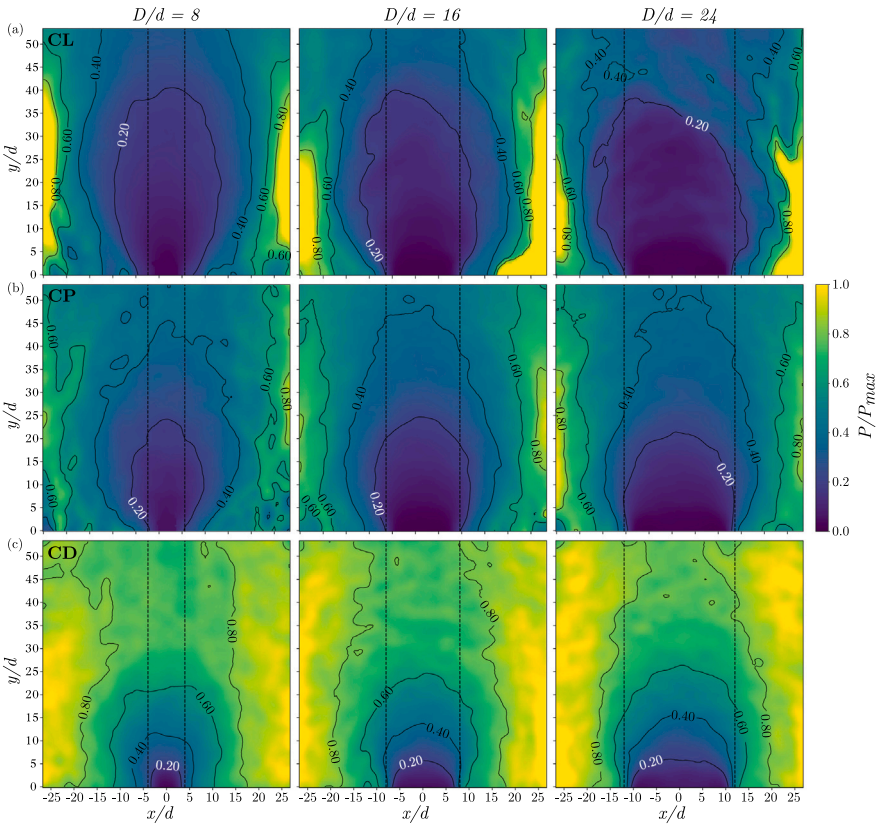

Fig. 7. Spatial distribution of the normalized mean local stress near the door for three aperture sizes, $D/d = 8, 16, 24$ (shown from left to right), and for the three configurations: (a) CL, (b) CP and (c) CD. The stress maps are scaled by the maximum stress measured in CL for $D/d = 24$, $P_{\max} = 70\,\mathrm{kN/m}$; black contours indicate iso-stress lines; vertical dashed lines show the opening size.

tensor is neglected because it is several orders of magnitude smaller than the contact stress, as also reported in [45].

Fig. 7 shows the mean local stress P, defined as the trace of the stress field $\sigma_{\alpha\beta}$, calculated within a window $W \times W$ at the outlet for three aperture sizes $D/d = 8, 16$ and 24, for the three configurations. The stress maps are scaled by the maximum stress measured in CL for $D/d = 24$: $P_{\max} = 70\,\mathrm{kN/m}$. The colormap ranges from dark blue (low stress) to bright yellow (high stress), allowing a direct visual comparison of the stress concentrations between door sizes and granular configurations; vertical dashed lines show the door size.

The stress fields exhibit a strong dependence on both particle shape and structural arrangement. Overall, CD sustains the highest mean local stresses close to the outlet, while CL shows the lowest values, with CP lying in between. These differences can be traced to the nature of interparticle contacts. In CD, contacts occur at isolated points, generating concentrated stress chains and a highly heterogeneous force network. In contrast, polygonal particles form extended face–face contacts that distribute forces over larger areas, producing a more uniform stress field [50,51]. Additionally, for particles of equal equivalent diameter, disks have a smaller effective contact area compared with polygons, which further amplifies local stress intensities in CD. This enhanced geometric interlocking in assemblies of polygonal grains also promotes arching, transferring a larger portion of the load onto the vertical walls of the silo. Consequently, stress concentrations along the walls are more pronounced in CL. In practice, these observations indicate that the CD configuration may overestimate stresses around the drawpoints, leading to conservative assumptions. Conversely, both CP and CD may underestimate stresses along the boundaries, eventually resulting in non-conservative assessments of dilution-triggering stresses in cave panels.

Another important observation concerns the influence of the outlet width D on the stress field, as illustrated by the iso-stress lines (black contours) in Fig. 7. Considering, for instance, the contour $P/P_{\max} = 0.2$ (highlighted in white) for a given configuration, the lateral extent of the iso-stress region increases proportionally with the outlet size, whereas its vertical extent remains essentially independent of D. This behavior can be attributed to the Janssen effect [52], whereby friction between the granular material and the silo walls supports part of the overburden weight, leading to a saturation of stresses with height. Consequently, the characteristic height of the stress field is governed primarily by particle properties and container geometry, rather than by the outlet dimensions. Nonetheless, the vertical extent of the stress-influenced region differs markedly among the three configurations: it is nearly an order of magnitude smaller in CL than in CD, while in CP it is approximately twice that observed in CL. This interpretation is again consistent with the Janssen effect, since polygonal particles exhibit geometric interlocking that enhances frictional support along the walls, causing the stress to saturate more rapidly with height than in the disk assembly [53]. The effect is logically more pronounced in the CL configuration, where the initial tessellated structure represents a highly dense and interlocked fragmented medium.

3.3. Caveability

To distinguish it from gravity flow, we use the term caveability to describe the tendency of an undercut rock mass to propagate a cave column upward through the orebody. Thus, evaluating caveability requires analyzing the relative particle velocities that develop within the silo during flow, rather than focusing solely on the outlet. Accordingly, the dynamical regimes generated in each configuration must be quantified for comparison. This can be achieved by examining the spatial variation of the local inertial number, computed as [54,55]

$$I = \frac{\dot{\gamma}\, d}{\sqrt{P/\eta}}, \tag{7}$$

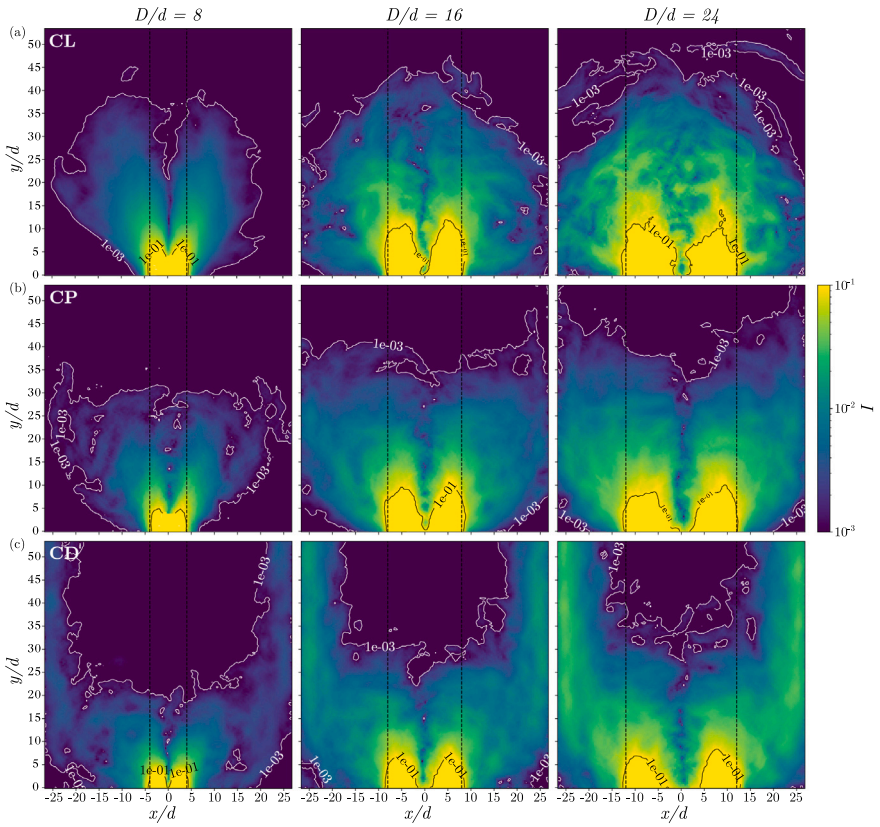

Fig. 8. Spatial distribution of the local inertial number, I, for three aperture sizes, $D/d = 8$, 16, 24 (shown from left to right), and for the three configurations: (a) CL, (b) CP, and (c) CD. The colormap ranges from dark purple (quasi-static regime, $I < 10^{-3}$) to light yellow (inertial regime, $I > 10^{-1}$). White and black contour lines denote these two threshold values, respectively. Vertical dashed lines show the opening size.

where $\dot{\gamma}$ is the local shear rate, P the local pressure, and d the mean particle diameter. The shear rate $\dot{\gamma}$ is obtained from the velocity field $\mathbf{V}(\mathbf{r}, t)$ through the two-dimensional strain-rate tensor. The components of this tensor are computed as

$$\dot{\epsilon}_{xx} = \partial_x \mathbf{V}_x, \qquad \dot{\epsilon}_{yy} = \partial_y \mathbf{V}_y, \qquad \dot{\epsilon}_{xy} = \frac{1}{2}\left(\partial_x \mathbf{V}_y + \partial_y \mathbf{V}_x\right),$$

and its scalar norm is defined as

$$\dot{\gamma} = \sqrt{2\left(\dot{\epsilon}_{xx}^2 + \dot{\epsilon}_{yy}^2 + 2\dot{\epsilon}_{xy}^2\right)}. \tag{8}$$

The velocity field itself is obtained using the coarse-graining formulation,

$$\mathbf{V}(\mathbf{r}, t) = \frac{1}{\rho(\mathbf{r}, t)} \sum_{i=1}^{N} m_i \, \mathbf{v}_i \, G\big(\mathbf{r} - \mathbf{r}_i(t)\big), \tag{9}$$

where m_i and $\mathbf{v}_i$ are the mass and velocity of particle i, and G is the coarse-graining kernel [45,48].

Fig. 8 shows the spatial map of I, calculated over the same $W \times W$ window at the outlet as the local pressure, for three outlet sizes. In the maps, $I < 10^{-3}$ and $I > 10^{-1}$ represent the quasi-static and dynamic flow limits [56], respectively, shown in color gradient from dark purple to light yellow. Black and white contours lines indicate these two threshold values of I, respectively. Vertical dashed lines show the opening size.

Starting with CL, high inertial values form a parabolic shape above the silo outlet. This indicates that particles predominantly slide collectively downward during most of the discharge, with relative motion (i.e., deconstruction of the tessellated block) becoming significant only near the outlet. This behavior can be explained by two factors preventing relative particle motion: (1) the polygonal shapes of the particles creating a geometric interlocking, and (2) the high initial packing fraction resulting in a fully interlocked system. Similarly to the pressure distribution, which is functionally related to I, the area affected by this dynamics scales with the width of the outlet but maintains a roughly constant vertical extent, regardless of the size of the opening. The quasi-static contours ($I < 10^{-3}$) in Fig. 8a demonstrate that arching develops as the cave roof forms. In practice, this dynamic configuration is responsible for the potential generation of air gaps within the cave.

In contrast, CD exhibits a markedly different behavior. Even for the smallest outlet sizes, high I values are observed not only near the outlet but also along the silo walls, indicating substantial relative motion between particles in these areas. Consequently, the upper regions of the silo do not discharge completely as a coherent block, suppressing arch formation—unlike the behavior observed in CL. Finally, CP shows an intermediate behavior. Although geometric interlocking is present due to the polygonal shapes, the relatively lower packing fraction allows the particles above the outlet to move more freely. This demonstrates the importance of considering both particle shape and packing density in the analysis of block-caving systems, as they significantly influence both local dynamics and stress distributions, which are critical for practical applications and flow control.

4. Conclusions

In this work, we investigated the discharge dynamics of granular silos as analogs for block caving systems. Using two-dimensional DEM Contact Dynamics simulations with rigid boundaries, we compared three configurations sharing the same particle size distribution but differing in shape and structural arrangement: a *caving-like* tessellated solid block into unbonded polygons (CL), a randomly deposited packing of the same polygons (*caving-polygons*, CP), and an equivalent system composed of disks (*caving-disks*, CD). This setup allowed us to isolate the influence of particle shape, interlocking, and initial fabric on outlet

flow, caveability and internal stress redistribution during discharge. The main findings of our study are the following:

- First, the global discharge behavior showed that all three configurations follow a Beverloo scaling, revealing a qualitatively similar gravity flow mechanism. However, the flow rates differed substantially: CD exhibited the highest discharge capacity, CP an intermediate one, and CL the lowest. These differences arise from particle interlocking and structural continuity, which opposes motion more effectively in the CL configuration.
- Second, the velocity profiles at the outlet displayed a consistent parabolic shape across all systems and collapsed onto a universal curve when rescaled by the central outlet velocity v_c. Despite significant differences in the magnitude of v_c, this collapse demonstrates that the overall dynamical behavior is preserved across all three cases.
- Third, the stress fields revealed markedly different internal mechanics. The CL assembly showed the most efficient stress redistribution, with forces transmitted through polygonal faces and supported laterally by the silo walls. Conversely, the CD configuration exhibited strong stress localization near the outlet. The CP system lay between these two extremes. These distinctions, absent in traditional silo analogs, are fundamental for understanding cave propagation and drawpoint pressure behavior.
- Finally, the inertial number field exposed clear contrasts in the internal rheology. The CL configuration maintained a cave-shaped quasi-static region above the outlet, with flow concentrated along a central channel and persistent interlocking in the upper portion of the column. In contrast, the CD assembly developed a broad dynamic zone surrounding the aperture, reflecting a more homogeneous and less constrained flow. The CP configuration again displayed an intermediate behavior, with partial interlocking but more diffuse dynamic regions than the CL case.

Overall, our results demonstrate that particle shape, fragmentation structure, and initial packing fabric exert a strong quantitative influence on discharge behavior, stress transmission, and local rheology, even though the fundamental kinematic scaling of silo flow remains unchanged. Although our numerical DEM tests rely on small-scale, idealized 2D conditions, the contrasting granular-flow kinematics observed across the three configurations can still inform future advances in caving models. The outcomes provide a basis for identifying DEM approaches that more accurately reproduce the kinematics and stress transfer mechanisms governing caving. Qualitatively, the strong divergences observed in stress redistribution indicate that assessments of rockburst initiation and drawpoint damage are less conservative than those obtained using traditional silo models when flow is driven by fragmentation, as in the CL configuration.

Despite these advances, direct experimental validation remains essential to quantitatively assess the predictive capability of the findings. Physical models of granular silos are well established in mining, powder technology and fundamental granular physics, yet controlling fragmentation and granular discharge experiments are extremely challenging. A perspective of this study is to implement fragmentation-driven DEM models to study the formation of isolated extracted zones, dilution and draw points interaction. Also, systematic sensitivity analyses, including particle-size polydispersity, frictional variability, anisotropic fracturing, and full 3D effects, are expected to further refine fragmentation-driven DEM approaches.

CRediT authorship contribution statement

Manuel Cárdenas-Barrantes: Writing – review & editing, Writing – original draft, Visualization, Validation, Software, Methodology, Investigation, Formal analysis, Conceptualization. **Mathieu Renouf:** Writing – review & editing, Writing – original draft, Software, Methodology, Investigation, Formal analysis, Conceptualization. **Emilien Azéma:** Writing – review & editing, Writing – original draft, Methodology, Investigation, Formal analysis, Conceptualization. **Carlos Ovalle:** Writing – review & editing, Writing – original draft, Supervision, Resources, Methodology, Investigation, Funding acquisition, Formal analysis, Conceptualization.

Declaration of Generative AI and AI-assisted technologies in the writing process

During the preparation of this work the authors used ChatGPT in order to improve the readability of the text.

Declaration of competing interest

The authors declare that they have no known competing financial interests or personal relationships that could have appeared to influence the work reported in this paper.

Acknowledgments

This study received financial support from the Natural Sciences and Engineering Research Council of Canada (NSERC) [projects ALLRP 568607-21 and ALLRP 590599-23], the Consortium de recherche et d'innovation en transformation métallique (CRITM) [project 2021-068], and the industrial partners of the Research Institute on Mines and Environment (RIME) UQAT–Polytechnique (irme.ca/en). The numerical simulations were enabled by computational resources provided by Calcul Québec and the Digital Research Alliance of Canada.

Data availability

Data will be made available on request.

References

[1] P. Darling, SME Underground, Society for Mining, Metallurgy, and Exploration (SME), 2023, URL https://app.knovel.com/hotlink/toc/id:kpSMEUMH01/sme-underground-mining/sme-underground-mining.
[2] B.H.G. Brady, E.T. Brown, Rock Mechanics for Underground Mining, third ed., Springer, Dordrecht, 2004, http://dx.doi.org/10.1007/978-1-4020-2113-3.
[3] D.H. Laubscher, Cave mining – state of the art, J. South Afr. Inst. Min. Met. 94 (10) (1994) 279–293.
[4] A. Campbell, Recovery and flow in cave mining: current knowledge gaps and the role of technology in the future, in: J. Wesseloo (Ed.), UMT 2020: Proceedings of the Second International Conference on Underground Mining Technology, Australian Centre for Geomechanics, 2020, pp. 77–104, http://dx.doi.org/10.36487/ACG_repo/2035_0.04, URL https://papers.acg.uwa.edu.au/p/2035_0.04_Campbell/.
[5] G. Chitombo, Cave mining — 16 years after laubscher's 1994 paper 'cave mining – state of the art', in: Y. Potvin (Ed.), Caving 2010: Proceedings of the Second International Symposium on Block and Sublevel Caving, Australian Centre for Geomechanics, 2010, pp. 45–61, http://dx.doi.org/10.36487/ACG_rep/1002_0.2_Chitombo, URL https://papers.acg.uwa.edu.au/p/1002_0.2_Chitombo/.
[6] E. Rubio, E. Widijanto, M. Bayuargo, Damage prediction in the extraction level of block caving mine: Case study in deep ore zone mine, PT freeport Indonesia, in: Proceedings of the 45th U.S. Rock Mechanics / Geomechanics Symposium, ARMA, San Francisco, USA, 2011, Paper ARMA 11-569.
[7] R. Castro, D. Oyarzo, R. Gómez, K. Suzuki, M. Cifuentes, Coupling geomechanical and gravity flow models to obtain more representative flow simulations and air-gap risk identification in caving mining, Int. J. Numer. Anal. Methods Geomech. 49 (1) (2025) 376–390, http://dx.doi.org/10.1002/nag.3880, arXiv:https://onlinelibrary.wiley.com/doi/pdf/10.1002/nag.3880. URL https://onlinelibrary.wiley.com/doi/abs/10.1002/nag.3880.
[8] J. Liu, C. Zhang, I. Canbulat, J. Oh, S. Saydam, A review of rockbursts associated with block caving, in: Proceedings of Caving 2022: Fourth International Conference on Block and Sublevel Caving, Australian Centre for Geomechanics, Online, 2022, pp. 1059–1074, http://dx.doi.org/10.36487/ACG_repo/2205_79.
[9] Y. Potvin, Empirical Open Stope Design in Canada (Ph.D. thesis), University of British Columbia, Vancouver, Canada, 1988.
[10] K. Suzuki Morales, F.T. Suorineni, B. Hebblewhite, Orebody cavability prediction challenges in block caving mining — a review, Bull. Eng. Geol. Environ. 83 (1) (2024) 23, http://dx.doi.org/10.1007/s10064-023-03516-6.

[11] F. Melo, F. Vivanco, C. Fuentes, Calculated isolated extracted and movement zones compared to scaled models for block caving, Int. J. Rock Mech. Min. Sci. 46 (4) (2009) 731–737, http://dx.doi.org/10.1016/j.ijrmms.2008.09.012.

[12] R.L. Castro, M.A. Fuenzalida, F. Lund, Experimental study of gravity flow under confined conditions, Int. J. Rock Mech. Min. Sci. 67 (2014) 164–169, http://dx.doi.org/10.1016/j.ijrmms.2014.01.013.

[13] H. Sun, A. Jin, D. Elmo, Y. Gao, S. Wu, A numerical based approach to calculate ore dilution rates using rolling resistance model and upside-down drop shape theory, Rock Mech. Rock Eng. 53 (2020) 4639–4652, http://dx.doi.org/10.1007/s00603-020-02180-6.

[14] V. Sánchez, R.L. Castro, S. Palma, Gravity flow characterization of fine granular material for block caving, Int. J. Rock Mech. Min. Sci. 114 (2019) 24–32, http://dx.doi.org/10.1016/j.ijrmms.2018.12.011, URL https://www.sciencedirect.com/science/article/pii/S1365160917309127.

[15] S. Jacobs, E. Kearsley, D. Cumming-Potvin, W. J., Modelling cave mining in the geotechnical centrifuge, in: In Physical Modeling in Geotechnics, the 9th International Conference on Physical Modelling in Geotechnics, (ICPMG 2018), CRC Press, 2018, pp. 809–814.

[16] F. Melo, F. Vivanco, C. Fuentes, V. Apablaza, Kinematic model for quasi static granular displacements in block caving: Dilatancy effects on drawbody shapes, Int. J. Rock Mech. Min. Sci. 45 (2) (2008) 248–259, http://dx.doi.org/10.1016/j.ijrmms.2007.07.005, URL https://www.sciencedirect.com/science/article/pii/S1365160907000913.

[17] V.T. Le, T.V. Nguyen, M. Karakus, G.D. Nguyen, H.H. Bui, SPH-based modelling of the entire rock caving process: insights into failure mechanisms, Int. J. Rock Mech. Min. Sci. 194 (2025) 106228, http://dx.doi.org/10.1016/j.ijrmms.2025.106228, URL https://www.sciencedirect.com/science/article/pii/S1365160925002059.

[18] A. Vyazmensky, D. Stead, D. Elmo, A. Moss, Numerical analysis of block caving-induced instability in large open pit slopes: A finite element/discrete element approach, Rock Mech. Rock Eng. 43 (1) (2010) 21–39, http://dx.doi.org/10.1007/s00603-009-0035-3.

[19] C. Guajardo, J. Jakubec, E. Esterhuizen, H. Pichuante, A. Thomas, The discrete fracture network–block caving fragmentation hybrid method: A new tool to assess fragmentation of block caving mining projects, in: Y. Potvin (Ed.), Caving 2022: Proceedings of the Fifth International Conference on Block and Sublevel Caving, Australian Centre for Geomechanics, 2022, pp. 927–938, http://dx.doi.org/10.36487/ACG_repo/2205_63, URL https://papers.acg.uwa.edu.au/p/2205_63_Guajardo/.

[20] P. Hamdi, D. Stead, D. Elmo, J. Töyrä, Use of an integrated finite/discrete element method-discrete fracture network approach to characterize surface subsidence associated with sub-level caving, Int. J. Rock Mech. Min. Sci. 103 (2018) 55–67, http://dx.doi.org/10.1016/j.ijrmms.2018.01.021, URL https://www.sciencedirect.com/science/article/pii/S1365160916304634.

[21] Y. Xu, K.D. Kafui, C. Thornton, G. Lian, Effects of material properties on granular flow in a silo using DEM simulation, Part. Sci. Technol. 20 (2) (2002) 109–124, http://dx.doi.org/10.1080/02726350215338, arXiv:https://doi.org/10.1080/02726350215338.

[22] H. Zhang, X. Zhang, G. Wang, X. Wang, J. Oh, G. Si, Fragmented rock block geometry affecting mechanical responses and fluid flow characteristics during compaction of caving zones, Powder Technol. 469 (2026) 121707, http://dx.doi.org/10.1016/j.powtec.2025.121707, URL https://www.sciencedirect.com/science/article/pii/S0032591025011027.

[23] P. Cundall, UDEC—ageneralized distinct element program for modelling jointed rock, Report PCAR-1-80, European Research Office, US Army Corps of Engineers, 1980.

[24] D. Cumming-Potvin, J. Wesseloo, M. Pierce, T. Garza-Cruz, L. Bouzeran, S. Jacobsz, E. Kearsley, Numerical simulations of a centrifuge model of caving, in: Y. Potvin, J. Jakubec (Eds.), Caving 2018: Proceedings of the Fourth International Symposium on Block and Sublevel Caving, Australian Centre for Geomechanics, 2018, pp. 191–206, http://dx.doi.org/10.36487/ACG_rep/1815_12_Cumming-Potvin, URL https://papers.acg.uwa.edu.au/p/1815_12_Cumming-Potvin/.

[25] R. McNearny, J. Abel, Large-scale two-dimensional block caving model tests, Int. J. Rock Mech. Min. Sci. Geomech. Abstr. 30 (2) (1993) 93–109, http://dx.doi.org/10.1016/0148-9062(93)90703-G, URL https://www.sciencedirect.com/science/article/pii/014890629390703G.

[26] P. Cavieres, S. Gaete, L. Lorig, P. Gomez, Three-dimensional analysis of fracturing limits induced by large scale underground mining at el teniente mine, in: Soil and Rock America, June 22 - 26, Cambridge, Massachusetts, 2003.

[27] B. Debnath, V. Kumaran, K.K. Rao, Dense granular flow through a flat-bottomed silo: Comparison of the DEM and continuum models with experiments, Powder Technol. 431 (2024) 119036, http://dx.doi.org/10.1016/j.powtec.2023.119036, URL https://www.sciencedirect.com/science/article/pii/S0032591023008197.

[28] W. Hancock, D. Weatherley, G. Chitombo, Large-scale simulations of gravity flow in block caving, in: Y. Potvin (Ed.), Caving 2010: Proceedings of the Second International Symposium on Block and Sublevel Caving, Australian Centre for Geomechanics, 2010, pp. 553–566, http://dx.doi.org/10.36487/ACG_rep/1002_38_Hancock, URL https://papers.acg.uwa.edu.au/p/1002_38_Hancock/.

[29] Q.-W. Liu, H.-L. Wang, R.-P. Chen, Z.-Y. Yin, X.-T. Lin, H.-N. Wu, Effect of relative density of 2D granular materials on the arching effect through numerical trapdoor tests, Comput. Geotech. 141 (2022) 104553, http://dx.doi.org/10.1016/j.compgeo.2021.104553, URL https://www.sciencedirect.com/science/article/pii/S0266352X21005322.

[30] Y.-S. Xie, Y.-S. Zhao, Numerical simulation of the top coal caving process using the discrete element method, Int. J. Rock Mech. Min. Sci. 46 (6) (2009) 983–991, http://dx.doi.org/10.1016/j.ijrmms.2009.03.005, URL https://www.sciencedirect.com/science/article/pii/S136516090900063X.

[31] C. Yi, D. Johansson, M. Wimmer, A. Nordqvist, J. Greberg, C. Rodriguez San Miguel, Numerical simulation of gravity flow in sublevel caving based on polyhedron DEM, Min. Met. Explor. 41 (1) (2024) 91–98, http://dx.doi.org/10.1007/s42461-023-00903-1.

[32] F. Dubois, M. Jean, LMGC90 une plateforme de développement dédiée à la modélisation des problèmes d'interaction, in: Actes Du Sixieme Colloque National En Calcul Des Structures, vol. 1, 2003, pp. 111–118.

[33] F. Dubois, M. Jean, M. Renouf, R. Mozul, A. Martin, M. Bagneris, Lmgc90, in: 10e Colloque National En Calcul Des Structures, 2011, pp. Clé–USB.

[34] F. Radjai, Contact dynamics method, Eur. J. Environ. Civ. Eng. 12 (7–8) (2008) 871–900, http://dx.doi.org/10.1080/19648189.2008.9693052, arXiv:https://doi.org/10.1080/19648189.2008.9693052.

[35] M. Renouf, F. Dubois, P. Alart, A parallel version of the non smooth contact dynamics algorithm applied to the simulation of granular media, J. Comput. Appl. Math. 168 (1) (2004) 375–382, http://dx.doi.org/10.1016/j.cam.2003.05.019, Selected Papers from the Second International Conference on Advanced Computational Methods in Engineering (ACOMEN 2002). URL https://www.sciencedirect.com/science/article/pii/S0377042703010021.

[36] R. Quey, P. Dawson, F. Barbe, Large-scale 3D random polycrystals for the finite element method: Generation, meshing and remeshing, Comput. Methods Appl. Mech. Engrg. 200 (17) (2011) 1729–1745, http://dx.doi.org/10.1016/j.cma.2011.01.002, URL https://www.sciencedirect.com/science/article/pii/S004578251100003X.

[37] M. Cárdenas-Barrantes, C. Ovalle, Multiscale insights into sliding surface liquefaction through DEM simulations, Comput. Geotech. 183 (2025) 107191, http://dx.doi.org/10.1016/j.compgeo.2025.107191, URL https://www.sciencedirect.com/science/article/pii/S0266352X25001405.

[38] D. Cantor, C. Ovalle, E. Azéma, Microstructural origins of crushing strength for inherently anisotropic brittle materials, Int. J. Solids Struct. 238 (2022) 111399, http://dx.doi.org/10.1016/j.ijsolstr.2021.111399, URL https://www.sciencedirect.com/science/article/pii/S0020768321004601.

[39] Y. Huillca, M. Silva, C. Ovalle, J.C. Quezada, S. Carrasco, G.E. Villavicencio, Modelling size effect on rock aggregates strength using a DEM bonded-cell model, Acta Geotech. 16 (3) (2021) 699–709, http://dx.doi.org/10.1007/s11440-020-01054-z.

[40] R. Arévalo, I. Zuriguel, Clogging of granular materials in silos: effect of gravity and outlet size, "Soft Matter" 12 (2016) 123–130, http://dx.doi.org/10.1039/C5SM01599E.

[41] Y.-Y. Liu, D.-L. Zhang, B.-B. Dai, J. Su, Y. Li, A.T. Yeung, Experimental study on vertical stress distribution underneath granular silos, Powder Technol. 381 (2021) 601–610, http://dx.doi.org/10.1016/j.powtec.2020.11.066, URL https://www.sciencedirect.com/science/article/pii/S0032591020311256.

[42] A. Hafez, Q. Liu, T. Finkbeiner, R.A. Alouhali, T.E. Moellendick, J.C. Santamarina, The effect of particle shape on discharge and clogging, Sci. Rep. 11 (1) (2021) 3309, http://dx.doi.org/10.1038/s41598-021-82744-w.

[43] A. Bignon, M. Renouf, R. Sicard, E. Azéma, Nonlinear effect of grain elongation on the flow rate in silo discharge, Phys. Rev. E 108 (2023) 054901, http://dx.doi.org/10.1103/PhysRevE.108.054901, URL https://link.aps.org/doi/10.1103/PhysRevE.108.054901.

[44] E. Goldberg, C. Manuel Carlevaro, L.A. Pugnaloni, Clogging in two-dimensions: effect of particle shape, J. Stat. Mech. Theory Exp. 2018 (11) (2018) 113201, http://dx.doi.org/10.1088/1742-5468/aae84b.

[45] S.M. Rubio-Largo, D. Maza, R.C. Hidalgo, Large-scale numerical simulations of polydisperse particle flow in a silo, Comput. Part. Mech. 4 (4) (2017) 419–427, http://dx.doi.org/10.1007/s40571-016-0133-4.

[46] W. Beverloo, H. Leniger, J. van de Velde, The flow of granular solids through orifices, Chem. Eng. Sci. 15 (3) (1961) 260–269, http://dx.doi.org/10.1016/0009-2509(61)85030-6, URL https://www.sciencedirect.com/science/article/pii/0009250961850306.

[47] A. Janda, I. Zuriguel, D. Maza, Flow rate of particles through apertures obtained from self-similar density and velocity profiles, Phys. Rev. Lett. 108 (2012) 248001, http://dx.doi.org/10.1103/PhysRevLett.108.248001, URL https://link.aps.org/doi/10.1103/PhysRevLett.108.248001.

[48] I. Goldhirsch, Stress, stress asymmetry and couple stress: from discrete particles to continuous fields, Granul. Matter 12 (3) (2010) 239–252, http://dx.doi.org/10.1007/s10035-010-0181-z.

[49] T. Weinhart, R. Hartkamp, A.R. Thornton, S. Luding, Coarse-grained local and objective continuum description of three-dimensional granular flows down an inclined surface, Phys. Fluids 25 (7) (2013) 070605, http://dx.doi.org/10.1063/1.4812809, arXiv:https://pubs.aip.org/aip/pof/article-pdf/doi/10.1063/1.4812809/15710430/070605_1_online.pdf.

[50] S. Carrasco, D. Cantor, C. Ovalle, P. Quiroz-Rojo, Shear strength of angular granular materials with size and shape polydispersity, Open Geomech. 4 (2023) 1–14, http://dx.doi.org/10.5802/ogeo.15, URL https://opengeomechanics.centre-mersenne.org/articles/10.5802/ogeo.15/.

[51] D. Cantor, E. Azéma, I. Preechawuttipong, Microstructural analysis of sheared polydisperse polyhedral grains, Phys. Rev. E 101 (2020) 062901, http://dx.doi.org/10.1103/PhysRevE.101.062901, URL https://link.aps.org/doi/10.1103/PhysRevE.101.062901.

[52] V.D. Ingenieure, Zeitschrift der Vereines Deutscher Ingenieure, vol. 39, Rudolph Gaertner, 1895.

[53] M.A. Hanif, D. van der Meer, Flow dynamics of different particle shapes in a rectangular silo, Phys. Rev. E 111 (2025) 025416, http://dx.doi.org/10.1103/PhysRevE.111.025416, URL https://link.aps.org/doi/10.1103/PhysRevE.111.025416.

[54] G.D.R. MiDi, On dense granular flows, Eur. Phys. J. E 14 (4) (2004) 341–365, http://dx.doi.org/10.1140/epje/i2003-10153-0.

[55] L. Lacaze, R.R. Kerswell, Axisymmetric granular collapse: A transient 3D flow test of viscoplasticity, Phys. Rev. Lett. 102 (2009) 108305, http://dx.doi.org/10.1103/PhysRevLett.102.108305, URL https://link.aps.org/doi/10.1103/PhysRevLett.102.108305.

[56] F. da Cruz, S. Emam, M. Prochnow, J.-N. Roux, F. Chevoir, Rheophysics of dense granular materials: Discrete simulation of plane shear flows, Phys. Rev. E 72 (2005) 021309, http://dx.doi.org/10.1103/PhysRevE.72.021309, URL https://link.aps.org/doi/10.1103/PhysRevE.72.021309.